Controlled coupling and characterization of oyster (*Crassostrea gigas*) ferritin with gold nanostars

Han Li[a], Xiaoyu Xia[a], Shuzhen Cheng[a], Jiachen Zang[b], Zhenyu Wang[a], Xianbing Xu[a], Ming Du[a,*]

[a] *School of Food Science and Technology, National Engineering Research Center of Seafood, Collaborative Innovation Center of Seafood Deep Processing, Dalian Polytechnic University, Dalian 116034, China*
[b] *College of Food Science and Nutritional Engineering, China Agricultural University, Beijing 100083, China*

A R T I C L E   I N F O

A B S T R A C T

Ferritin has good thermal stability, resistance to certain acids and bases, and targeting, and has broad application prospects in the synthesis of gold nanostars (AuNS). In this study, we screened monodisperse AuNS with uniform particle size and morphology through a one-step synthesis method and coupled the synthesized AuNS with oyster ferritin (GF1). The results showed that the surface plasmon resonance (SPR) peaks of the coupled GF1@AuNS changed significantly, and the changes in infrared spectra and potential confirmed the success of the synthesis, while the microscopic morphology showed an increase in particle size and surface peak coverage. Furthermore, GF1@AuNS does not induce cell death in the 100 µmol/L range, is highly stable in physiological environments, and exhibits good X-ray attenuation in micro-computed tomography. Due to the unique functional activity of ferritin and AuNS, GF1@AuNS has potential applications in food detection and drug development in the future.

1. Introduction

With the development of nanotechnology, the unique physical, chemical, and optical properties of nano-sized gold nanoparticles have attracted more and more attention[1]. Gold nanoparticles have the advantages of easy synthesis, good chemical compatibility, good stability, and easy surface coupling, with promising medical imaging and targeted drug delivery applications[2]. Gold nanostars (AuNS) are nanoparticles with a central core and many irregular tips. The presence of sharp edges and branch angles make nanoparticles exhibit good surface electric field enhancement and have better optical properties[3-4]. At the same time, AuNS has good X-ray attenuation characteristics, unique optical properties, and absorption characteristics in the near-infrared region, and can be used as a computed tomography (CT) imaging contrast agent, showing potential application prospects[5-6]. The synthesis of AuNS mainly adjusts its size and morphology by metal salts, reducing agents, or others in the reaction system[7-8]. According to the different reaction steps, the synthesis methods of AuNS can be divided into one-step synthesis method and Au seed growth method[9-11]. Now, a controllable and simple method for the synthesis of AuNS with good monodispersity and uniform morphology is required.

The stability of AuNS is extremely important during synthesis, storage, and use. Because AuNS is prone to aggregation and precipitation, the surface of AuNS is often modified to improve stability and biocompatibility, so modification of AuNS with macromolecules with specific functional properties has potential research value[12-15]. Piersandro et al.[16] found that sulfhydryl polyethylene glycol (PEI-SH) has unique advantages in stabilizing AuNS, which can significantly improve its colloidal stability. Li et al.[17]
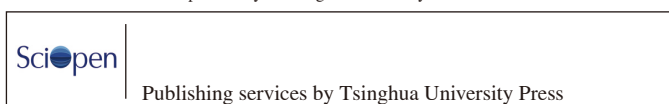
used a naturally derived polymer, bovine serum albumin (BSA), as an excellent substitute to modify AuNS, and the modified AuNS showed good colloidal stability and biocompatibility.

Ferritin is a non-toxic iron storage protein widely found in living organisms, consisting of a protein shell surrounding an iron core consisting of iron and phosphate molecules with outer and inner diameters of 12 and 8 nm, respectively[18-20]. Ferritin has strong stability such as resistance to dilute acids (pH 2.0), dilute bases (pH 12.0), and higher temperatures (70 °C), and has good monodispersity and biocompatibility[21-22]. The amino acid composition of ferritin is abundant, which provides certain advantages for binding AuNS. So far, the study of coupling ferritin with gold nanoparticles has attracted attention, which provides a new way of thinking for our research. Current major research is on the incorporation of nanoparticles into this modified ferritin cavity[23-26]. However, due to the easy aggregation of bare AuNS, surface functionalization is required to increase colloidal stability and biocompatibility to improve the application of AuNS. Our study aimed to bind ferritin to the surface of AuNS to give it some activity and reduce aggregation to improve stability.

In this study, the best means of AuNS synthesis were screened, and this was used as a basis for further screening the coupling mode between ferritin and AuNS, followed by structural characterization and identification of GF1@AuNS. We found that GF1@AuNS has homogeneous particle size distribution and distinct structural characteristics, and has good biocompatibility and stability. The gray value measurements on micro-CT showed a clear linear trend between the X-ray attenuation coefficient and concentration. The above findings provide an important theoretical basis for future food testing and drug development of GF1@AuNS.

2. Materials and methods

2.1 Materials and reagents

Fresh oyster (*Crassostrea gigas*) was obtained from the local market (Dalian, China). Gold (III) chloride ($HAuCl_4$), silver nitrate ($AgNO_3$), *L*-ascorbic acid, and sodium citrate ($C_6H_5Na_3O_7$) were purchased from Sigma-Aldrich (St. Louis, MO, USA). Ammonium sulfate, Tris-HCl, and DEAE-Sepharose were purchased from Sigma Chemical Co. (St. Louis, MO, USA). HFF-1 cell, B16F10 cell, and corresponding medium were obtained from Procell Life Science & Technology Co., Ltd. (Wuhan, China). Milli Q Plus 185 purification system (Millipore, Billerica, MA, USA) was used for all chemicals and reagents for experiments.

2.2 Synthesis and characterization of AuNS

AuNS-1 was synthesized using a one-step synthesis method with some modifications[27]. Here, 360 µL of 10 mmol/L $HAuCl_4$ and 20 µL of 10 mmol/L $AgNO_3$ were added to 10 mL of H_2O and vortexed quickly for 30 s, followed immediately by 60 µL of 100 mmol/L $C_6H_8O_6$ and vortexed for 30 s. After the solution turned blue-green, the synthesized sample was centrifuged at low speed for 1 h and resuspended in 1 mL of H_2O.

AuNS-2 was synthesized using the method of Au seed growth synthesis with some modifications[28-30]. Take 10 mL of 1% $HAuCl_4$ to heat and boil, add 1 mL of 1% $C_6H_5Na_3O_7$, continue to heat and boil

for 20 min, and cool to room temperature to prepare Au seed solution. Add 100 mmol/L $HAuCl_4$ to the reaction flask and continue stirring, then add Au seed solution, 1% $C_6H_5Na_3O_7$ and 33 mmol/L $C_6H_6O_2$ sequentially. After the solution turned blue-green, the synthesized samples were centrifuged at low speed for 1 h and resuspended in 1 mL of H_2O. The AuNS samples prepared above were stored at 4 °C before the next experiment.

2.3 Conjugation of GF1 on AuNS

Oyster RNA was extracted from fresh oysters using TRIzol, and ferritin gene *GF1* was obtained by reverse transcription and polymerase chain reaction (PCR) amplification. *GF1* was then cloned into the expression plasmid pET21a and verified by DNA sequencing. BL21-pET21a-GF1 was transferred into LB medium for expanding culture. Ferritin-expressing *E. coli* BL21 was obtained by centrifuging the medium, sonicated in an ice bath, and the treated solution was centrifuged at 12 000 × *g* for 10 min to collect the supernatant. The supernatant was then heated at 50 °C for 10 min to denature proteases and other heat-sensitive proteins. Purification of oyster ferritin was carried out using ammonium sulfate precipitation and ion exchange chromatography (DEAE-Sepharose Fast Flow column)[31]. The purified oyster ferritin (GF1) was stored at –20 °C to maintain protein structure and activity.

GF1@AuNS-1 was synthesized by direct coupling. The different concentrations of GF1 solutions (10, 20, 40, 60, 80, and 100 µg/mL) diluted with ultrapure water was coupled with AuNS at 37 °C with continuous stirring for 1 h[32]. GF1@AuNS-2 was synthesized using carbodiimide (EDC) with BSA as an intermediate reactant. BSA was first dissolved in phosphate buffered saline (PBS, pH 5) to promote effective cross-linking. Then EDC was added to BSA and stirred continuously at 4 °C for 5 min to activate the carboxylate group on BSA. GF1 dissolved in PBS (pH 5) was then mixed with the BSA-EDC solution and stirred at 4 °C for 12 h, followed by dialysis with PBS (pH 5) to remove the intermediate product and excess EDC. BSA-GF1 was then coupled to AuNS by non-specific adsorption at 37 °C with continuous stirring for 1 h[33].

2.4 Structure characterization of AuNS and GF1@AuNS

Dynamic light scattering (DLS, LS Instruments, Switzerland) was used to determine the particle size distribution of synthesized samples[34]. The sample was diluted to the appropriate concentration with ultrapure water and then dusted before determination. The measurement was carried out at 90° and the measurement time was set as 20 s. The measured data were fitted and the average particle size was obtained by the Conti algorithm. Using the pipette, 50 µL of samples were diluted into a solution with ultrapure water, and ultrapure water was used as the control for scanning in the wavelength range of 400–900 nm by ultraviolet (UV)-visible absorption spectrum (Lambda 35, Perkin Elmer, Massachusetts, USA)[35]. Freeze-dried sample powder (2 mg) was mixed with dried KBr (100 mg) and then pressed into the sample disk for infrared spectrum analysis on a Fourier transform infrared spectrometer (Perkin Elmer, Waltham, USA)[36]. The resolution is set to 4 cm^{-1} and the measurement range is 400–4 000 cm^{-1}. The Zeta potential of AuNS and GF1@AuNS was determined using a laser particle scanning

analyzer (Dispersion Technology, Inc., Bedford Hills, USA). After correction using the calibration solution, the solution was measured 3 times to avoid experimental errors[37].

2.5 Morphological analysis of AuNS and GF1@AuNS

Sample (AuNS and GF1@AuNS, 10 μL) was diluted to 100 μL with ultrapure water, and then the prepared sample was dropped onto a smooth surface. The carbon film was covered on the surface of the droplet, and the droplet was naturally adsorbed by the interaction force. After natural drying, transmission electron microscopy (TEM, JEM-2100, JEOL, Japan) was used for observations with an acceleration voltage of 200 kV, and observations by atomic force microscope (AFM-5500M, Hitachi, Tokyo, Japan) were made in different areas to avoid experimental errors in both heights retrace mode and phase retrace mode[38]. The samples were diluted 10 times with ultrapure water and 10 μL of liquid was dropped onto the surface of the mica for observation. The probe was scanned on the mica at a rate of 1 Hz with a drive frequency of 336.3 kHz[39]. For scanning electron microscopy (SEM, SU8010, Hitachi, Tokyo, Japan), the glass slides were first modified to adsorb samples. Clean slides were placed in 1 mol/L NaOH for 12 h, rinsed briefly with ultrapure water, then placed in 1 mol/L HCl for 1 h and left to dry. Samples were dropped onto glass slides and fixed on the sample stage and treated with gold spray for 60 s before being measured[40].

2.6 Cell cytotoxicity analysis of AuNS and GF1@AuNS

In vitro incubated HFF-1 and B16F10 cells were used as models to evaluate the effect of prepared AuNS and GF1@AuNS nanomaterials on cell viability. Cells were cultured in a cell incubator at 37 °C and 5% CO_2 for optimal growth conditions. After adjusting cell conditions, cells were seeded into 96-well culture plates (5×10^4 cells/well). After the cells were grown adhering to the wall, the medium was discarded and 200 μL of medium containing AuNS and GF1@AuNS (concentrations of 0.2, 0.4, 0.6, 0.8, and 1.0 mmol/L, actually the concentration of Au determined by ICP-OES) was used to subculture at 37 °C and 5% CO_2 for 1 h and 24 h. Then, 20 μL of CCK-8 was added to the culture plate, and incubation was continued at 37 °C for 1 h. The absorbance value was measured at 450 nm using a microplate reader to calculate the cell viability.

2.7 Stability analysis of AuNS and GF1@AuNS

Equal amounts of AuNS and GF1@AuNS solutions were resuspended in the same volume of deionized water and saline, and 4 sets of samples were taken at 12 and 24 h for UV-visible absorption spectrum (Lambda 35, Perkin Elmer, Massachusetts, USA), respectively.

2.8 X-ray attenuation coefficient of GF1@AuNS

The concentration of Au in the GF1@AuNS solution was determined by inductively coupled plasma emission spectroscopy (ICP-OES, PerkinElmer, Massachusetts, USA). Aqueous solutions with Au concentrations of 0.2, 0.4, 0.6, 0.8, and 1.0 mmol/L were prepared in 2 mL ultrapure water and placed in EP tubes. Determination of the X-ray attenuation capacity of GF1@AuNS using the micro-CT system (SKYSCAN1272, Bruker, Germany). The X-ray tube voltage and current are set to 120 kV and 100 mA, respectively.

3. Results and discussions

3.1 Results of synthesis and screening of AuNS

With continuous improvements in the preparation of anisotropic nanostructures, inorganic particles can be grown *in situ* in the branched structure of AuNS. The most critical aspect of the one-step synthesis is the determination of the appropriate reducing agent, reactant concentration, and reaction time. In addition, the synthesis of AuNS with monodisperse properties by Au seed synthesis is also a common method. The differences in color and optical properties of AuNS are largely due to the differences in particle size and morphology so slight changes in size and shape can lead to significantly different interactions between AuNS.

In this study, we used 2 commonly used methods for the synthesis of AuNS. As shown in Fig. 1, the TEM results showed the synthesis of AuNS-1 but with a non-uniform morphology (Fig. 1A), while the particle size results showed different size distributions of the synthesized particles, with AuNS-1 having particle sizes of 1.58, 4.86, and 83.18 nm and branch lengths ranging 10–60 nm (Fig. 1B). Our goal is to synthesize monodisperse AuNS with uniform particle size and branching for easy surface modification. This AuNS has greater stability and exhibits good SERS performance[41-42]. Due to the obvious differences in the microstructure and particle size of AnNS-1, another synthesis method was selected.
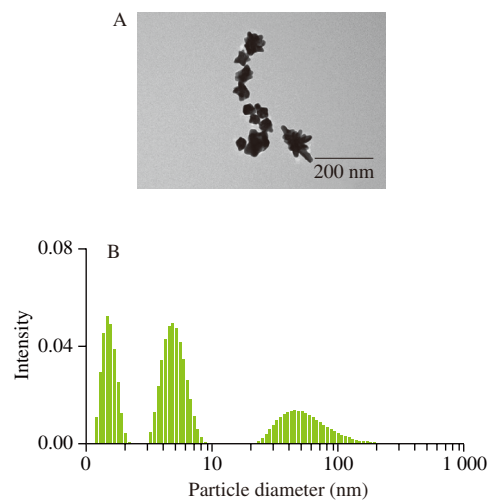
Fig. 1 Morphological characterization and dispersibility of AuNS-1 prepared by one-step synthesis method. (A) TEM image of AuNS-1. (B) Particle size distribution of AuNS-1.

The first step in the Au seed growth synthesis method is to use $HAuCl_4$ as raw material and reduce it with $C_6H_5Na_3O_7$ at room temperature to synthesize smaller particle-sized seeds. The second step of gold nucleation growth was synthesized using $HAuCl_4$ as the raw material and $C_6H_6O_2$ as the reducing agent, with the addition of $C_6H_5Na_3O_7$ as the assistant agent. The effect of different contents of Au seed, $HAuCl_4$, and $C_6H_6O_2$ on the synthesis of AuNS-2 was

screened by UV-visible spectrum. The Au seed gradually changed from purple to blue-green (picture of sample bottles of Figs. 2A–C). The main reason for the change in color of the nanoparticles is the change in their local surface plasmon resonance (LSPR). When light is irradiated on nanoparticles of different sizes and shapes composed of precious metals, the LSPR changes, leading to a change in the position of the maximum absorption peak in the UV-visible spectrum, and the gold nanoparticles grow into a stable star shape. It has been reported that changing the volume of Au seed, HAuCl₄, and reducing agents in the reaction system can change the final morphology of the AuNS[43]. The results showed that the absorption of Au seed had a maximum absorption peak of 520 nm, while AuNS-2 was all around 600 nm, which showed a significant red shift, proving the successful synthesis of AuNS-2 (Figs. 2A–C). The peak shape of the UV-visible absorption spectrum can also be used to characterize the particle size distribution. If the peak shape is symmetrical and the half-peak width is narrow, the particles are uniform in shape and size and well dispersed, so the best synthesis conditions are Au seed (80 μL), HAuCl₄ (25 μL), and C₆H₆O₂ (1 000 μL). The synthesized AuNS-2 was observed to have multiple tips under TEM with an average peak density of about 10 and an average length of about 20 nm (Fig. 2D). The DLS results showed a homogeneous particle size distribution with a particle size of about 70 nm (Fig. 2E). It has been shown that AuNS has a higher surface-enhanced Raman scattering (SERS) enhancement effect than gold nanospheres or gold nanorods[44-45]. Therefore, it is hypothesized that size and morphology have a significant effect on SERS enhancement[32,41]. Therefore, AuNS-2 synthesized by optimizing the experimental method was chosen for subsequent experiments.

3.2　Coupling and characterization of GF1@AuNS

The binding modes of AuNS-2 and proteins are mainly divided into 2 types, the first is non-covalent adsorption, and the second is chemical covalent binding. Direct coupling is non-covalent adsorption, as shown in Figs. 3A and B, directly coupled GF1@AuNS-1 has similar morphology, uniform particle size, and good monodispersity. This is due to the spiky surface of the AuNS increasing the surface area for non-covalent adsorption of GF1, resulting in a larger GF1 payload on each AuNS. However, the TEM background of GF1@AuNS-2, obtained by chemical covalent binding, was complex, demonstrating the presence of other intermediate products, together with some variation in particle size (Figs. 3C and D). The direct coupling product GF1@AuNS-1 was therefore chosen for subsequent experiments.

The coupling of GF1 to AuNS-2 (GF1@AuNS-1) was performed according to the synthesis described above and the structure was determined to verify the success of the synthesis. The UV-visible spectrum showed an SPR absorption peak of about 620 nm for AuNS-2, but AuNS-2 coupled to GF1 showed a significant quenching of fluorescence and the corresponding peak pattern disappeared (Fig. 4A). Also, the sample bottle pictures in the upper left of Fig. 4A showed that the blue-green color of the AuNS-2 becomes essentially colorless after coupling, also verifying that the tips of the AuNS-2 surface are covered. The structure of GF1@AuNS-1 was further verified by infrared spectra, and the results were shown in Fig. 4B. Characteristic peaks of GF1@AuNS-1 are similar to those of GF1 but different from those of AuNS-2, suggesting that GF1 may be adsorbed at the tip of AuNS-2. Some peaks of GF1@AuNS-1 were shifted compared to GF1. The shift from 1 657 to 1 630 cm⁻¹ may be caused by the combination of AuNS-2 and amide I groups, while the shift from 3 309 to 3 440 cm⁻¹ represents the formation of hydrogen bonds. The characteristic peaks of AuNS-2 are mainly distributed in the regions of 3 195, 1 403 and 1 115 cm⁻¹. These peaks almost disappear in the GF1@AuNS-1 spectrum due to the restriction of stretching and bending vibrations of AuNS-2 molecules. This may be because the tip of AuNS-2 is completely covered by GF1. At the same time, the peaks in the overall infrared spectrum of
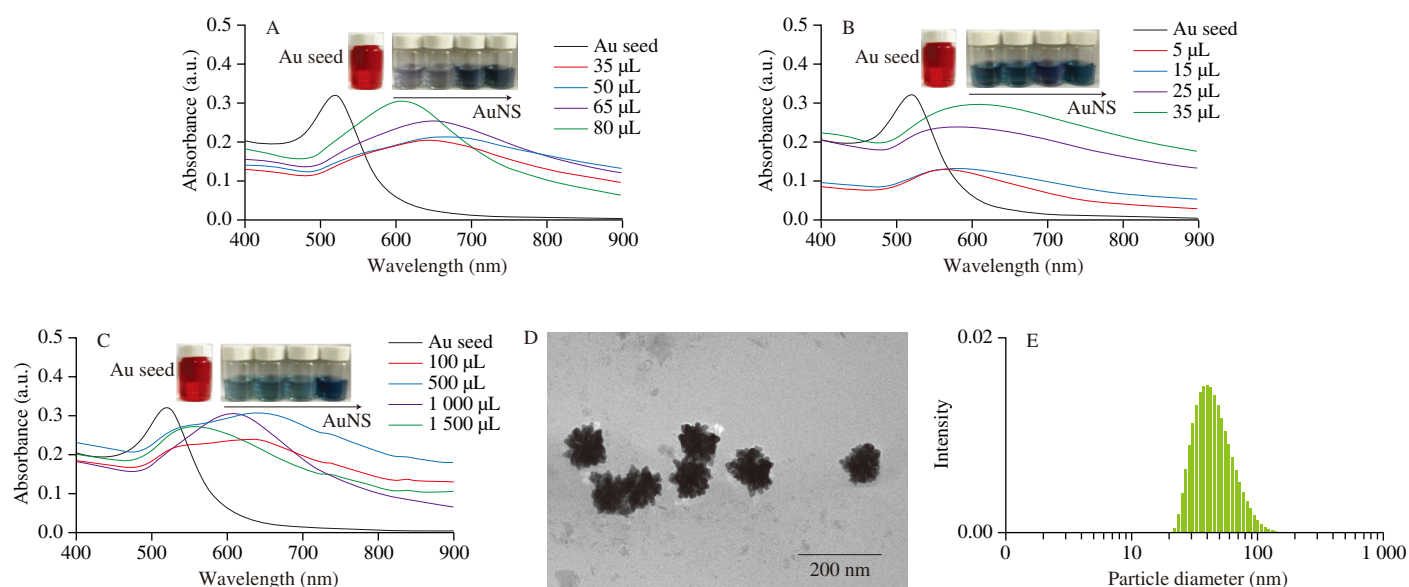
Fig. 2　Screening and characterization of AuNS-2 prepared by Au seed synthesis method. (A) The UV-visible absorption spectrum of AuNS-2 synthesized by adding different content of Au seed. (B) The UV-visible absorption spectrum of AuNS-2 synthesized by adding different content of HAuCl₄. (C) The UV-visible absorption spectrum of AuNS-2 synthesized by adding different content of C₆H₆O₂. (D) TEM image of AuNS-2. (E) Particle size distribution of AuNS-2.
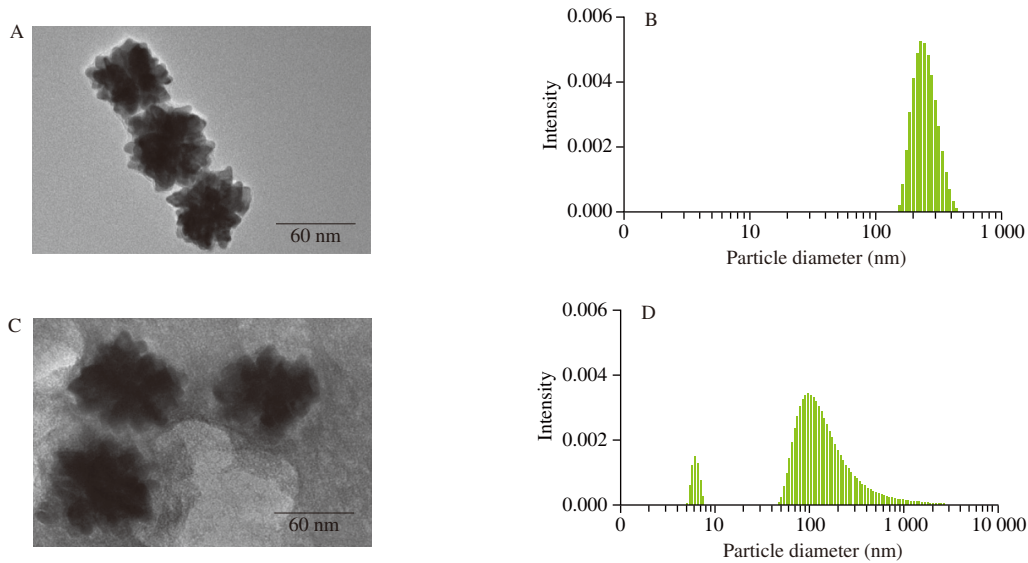
Fig. 3 Morphological characterization and dispersibility of different coupling methods between GF1 and AuNS. (A) TEM image of GF1@AuNS-1. (B) Particle size distribution of GF1@AuNS-1. (C) TEM image of GF1@AuNS-2. (D) Particle size distribution of GF1@AuNS-2.
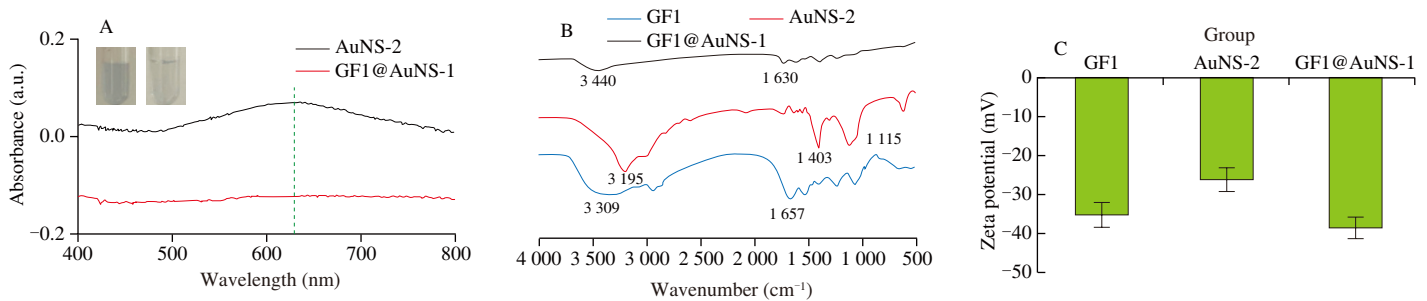
Fig. 4 The structural characterization of GF1, AuNS-2 and GF1@AuNS-1. (A) The UV-visible absorption spectrum of AuNS-2 and GF1@AuNS-1. (B) The infrared spectra of GF1, AuNS-2 and GF1@AuNS-1. (C) Zeta potential of GF1, AuNS-2 and GF1@AuNS-1.

GF1@AuNS-1 appear significantly diminished, indicating that GF1 has been successfully modified on the surface of the AuNS-2. The surface potential of AuNS-2 is approximately –26.3 mV, while the surface potential of GF1@AuNS-1 is about –38.8 mV due to the inherently negative electrical properties of GF1 (Fig. 4C). Recent experimental findings indicate that reducing the surface charge of the synthesized nanoparticles enhances the colloidal stability and reduces toxicity. Consequently, the coupling of oyster ferritin with AuNS-2 is expected to result in improved stability and reduced toxicity[46].

3.3 Micromorphological characterization of GF1@AuNS-1

The results of the above study were used to synthesize GF1@AuNS-1, a coupling substance between GF1 and AuNS-2. Compared with unmodified AuNS-2, the surface protein layer of GF1@AuNS-1 observed under TEM did not change significantly, especially the crystalline nature of Au, so further micromorphological characterization of the above successfully synthesized AuNS-2 and GF1@AuNS-1 was carried out. AFM can be used to obtain information on the structure of surface topography and roughness at nanometer resolution through force distribution information. The results showed that the individual AuNS-2 has a dispersed particle structure, all of which are spherical in shape (Fig. 5A). In contrast,

GF1@AuNS-1 was uniformly distributed in selected areas with significantly larger particle sizes, but no significant agglomeration was observed (Fig. 5B). As can be seen from the height analysis in the upper right corner of the image, the size of GF1@AuNS-1 is about 60 nm, an increase of about 30 nm compared to the unmodified AuNS-2 (about 30 nm). Changes in the size of the nanoparticles indirectly indicated the success of the modification of the surface proteins. SEM is the process of converting different features of a sample surface into a video signal sequentially and proportionally, thus observing images of various features on the surface of the sample. As shown from Fig. 5C, the AuNS-2 prepared by the Au seed growth method is very homogeneous in size. In addition, the surface of the prepared AuNS-2 contains a large number of dendritic structures, which also contribute to the red shift of the peak position. The SEM results of GF1@AuNS-1 showed the disappearance of the dendritic structure and a smooth surface, indicating that GF1 is grafted onto the AuNS-2 surface, forming core-shell nanoparticles (Fig. 5D).

3.4 Cell cytotoxicity, stability, and X-ray attenuation coefficient of AuNS and GF1@AuNS

Measuring cell viability after adding nanomaterials, it reflects the evaluation of cell injury *in vitro*. HFF1 cells are normal healthy cells
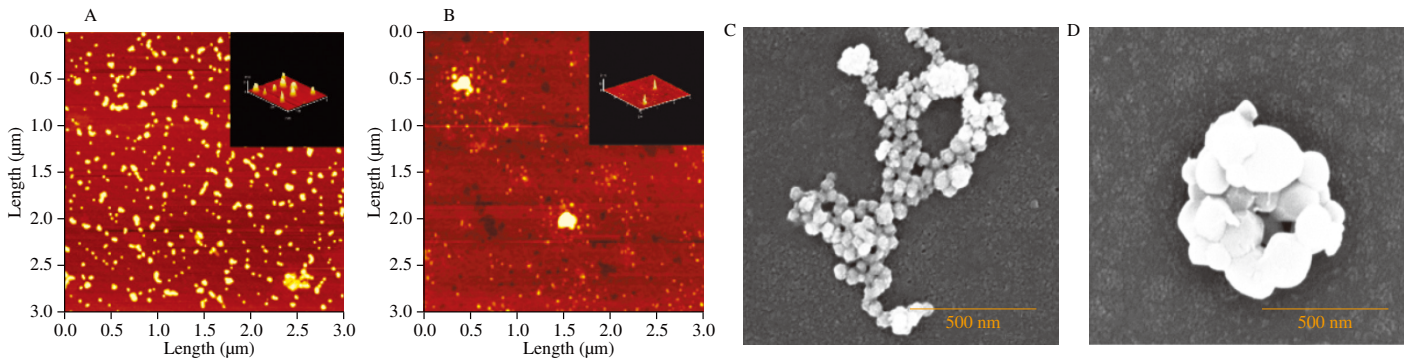
Fig. 5 The micromorphology of AuNS-2 and GF1@AuNS-1. (A) AFM image of AuNS-2. (B) AFM image of GF1@ AuNS-1. (C) SEM image of AuNS-2. (D) SEM image of GF1@ AuNS-1.
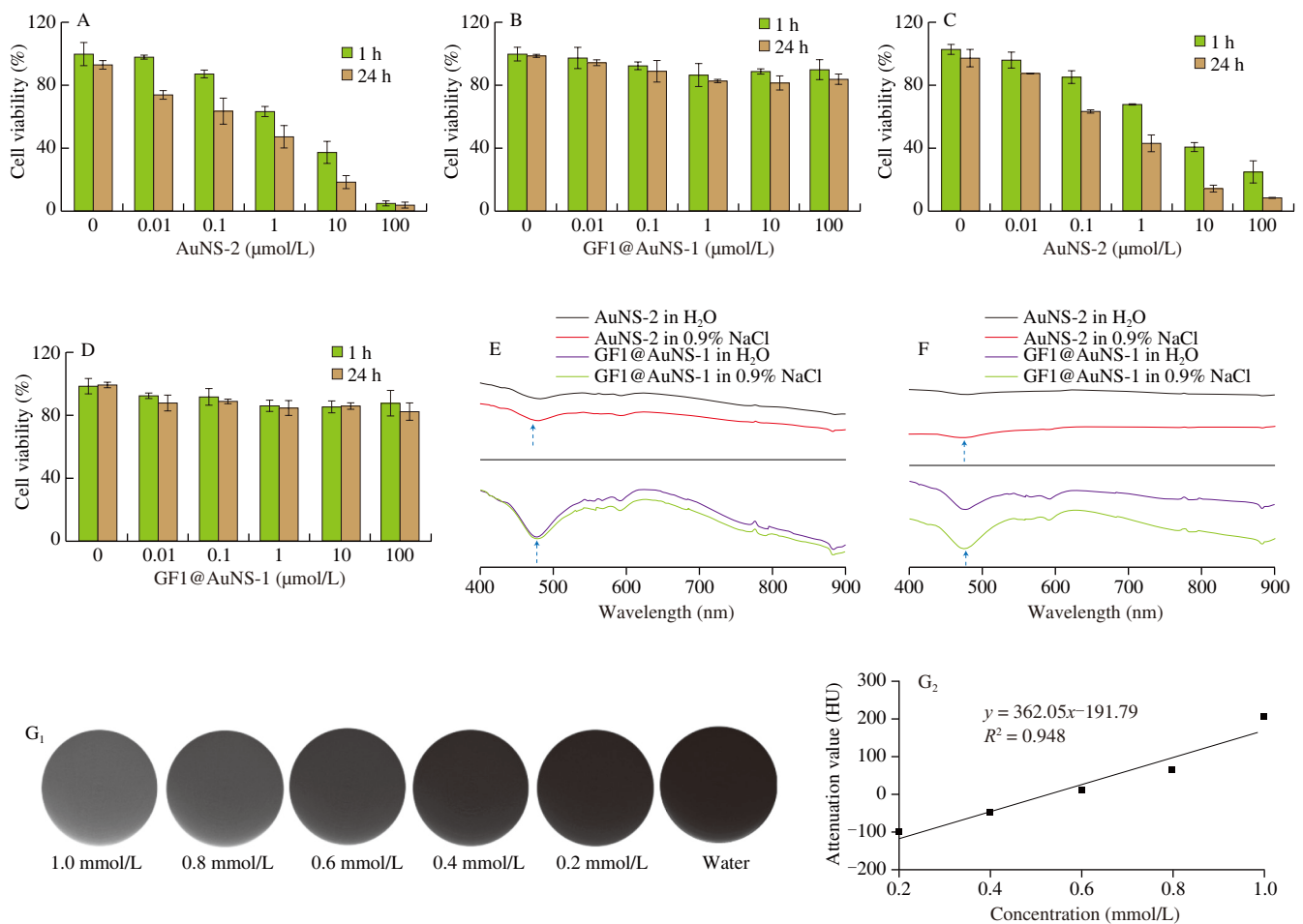
Fig. 6 Cell cytotoxicity, stability, and X-ray attenuation coefficient of AuNS-2 and GF1@AuNS-1. Cells were cultured for 24 h, treated with AuNS-2 and GF1@AuNS-1 for 1 and 24 h respectively, and cell viability was measured using CCK8. HFF-1 cells treated with (A) AuNS-2 and (B) GF1@AuNS-1. B16F10 cells treated with (C) AuNS-2 and (D) GF1@AuNS-1. The UV-visible absorption spectrum of AuNS-2 and GF1@AuNS-1 in deionized water and saline environments at (E) 12 and (F) 24 h. (G) CT images and attenuation values of GF1@AuNS-1.

that can maintain the undifferentiated state of embryonic stem cells. B16F10 cells are a kind of spontaneous tumor cells in mice, which can be considered ideal cells for designing tumor models. CCK-8 is used to examine the cell viability induced by AuNS-2 and GF1@AuNS-1 in two cells (Figs. 6A–D). When the concentration of AuNS-2 (actually the concentration of Au) was higher than 0.1 µmol/L, both cells showed significant cytotoxicity (survival rate below 80%).

Increasing the AuNS-2 concentration to 10 µmol/L resulted in a cell survival rate of around 20%, which showed a concentration-dependent trend. On the other hand, the concentration of GF1@AuNS-1 in the range of 0 to 100 µmol/L showed no significant cytotoxicity (survival above 80%) for either cell. This suggests that GF1@AuNS-1 can significantly reduce the cytotoxicity of AuNS-2 in a certain range of concentrations.

As a contrast agent for CT imaging, AuNS-2 inevitably appears in physiological environments such as culture medium. Aggregated AuNS-2 has a major impact on its optical properties and CT images[47]. This requires AuNS-2 to be highly stable and exhibit good distribution in physiological environments. Therefore, the stability in deionized water versus saline needs to be determined by the UV-visible spectrum. The results were shown in Figs. 6E and F (12 and 24 h). After GF1@AuNS-1 was resuspended in deionized water and normal saline for 12 h, the spectrum did not change significantly. However, the spectrum of AuNS-2 dispersed in saline solution showed quenching, indicating that its dendritic structure was disrupted and some aggregation occurred. After 24 h, both AuNS-2 and GF1@AuNS-1 were quenched to a certain extent, but the quenching degree of AuNS-2 was greater. The above experimental phenomenon shows that oyster ferritin coupling to AuNS-2 enhances the stability of AuNS-2. Li et al.[17] used BSA to modify gold nanoparticles (AuNPs), and the modified AuNPs showed good colloidal stability and biocompatibility, which was similar to our conclusion.

Micro-CT is the imaging of the attenuation of X-rays by an object, resulting in a grey-scale image. The main CT contrast media currently in clinical use are compounds containing iodine molecules, such as iohexol. The iodine contrast media has a very short retention time in the body and can be quickly cleared by the body's scavenging system, but it has a long retention time in the kidneys, which has certain side effects on the kidneys, and the iodine contrast media is non-specific and cannot specifically identify the tumor site[48]. Therefore, the search for new materials that effectively prolong the retention and imaging time in circulation, very low cytotoxicity, and toxic effects on the kidney for CT contrast media has been a focus of research[49]. Therefore, we need to investigate the imaging effects of nanomaterials with specific functions following the coupling of AuNS-2 with ferritin (GF1@AuNS-1). As shown in Fig. 6G, CT images and attenuation values (hounsfiled unit) showed that GF1@AuNS-1 has a strong X-ray attenuation capability, and the CT value of GF1@AuNS-1 increased with increasing concentration and was linearly correlated. In addition, the high image contrast, clear imaging, and high brightness demonstrated that the use of GF1@AuNS-1 as a CT contrast media can well improve the disadvantages of existing contrast media when applied to existing CT imaging systems.

4. Conclusion

In recent years, AuNS, with its special optical properties and surface chemical affinity, has received increasing attention for its great advantages in imaging, diagnosis, and therapy. Hence, modifying AuNS with ferritin allows targeting and other unique functional activities. In this study, AuNS was prepared by Au seed synthesis, and functional gold nanomaterials (GF1@AuNS) were prepared by coupling AuNS with ferritin. Samples were characterized by particle size distribution, micromorphology, and optical properties before and after synthesis. GF1@AuNS had no significant cytotoxicity to cells in the range of 1–100 μmol/L, and high stability in a physiological environment. Micro-CT results also showed that GF1@AuNS has good X-ray attenuation and imaging capabilities. The results of these studies provide a theoretical basis for exploring a novel means of food detection and drug development.

Declaration of competing interest

Ming Du is an editorial board member for *Food Science and Human Wellness* and was not involved in the editorial review or the decision to publish this article. The authors declare that they have no known competing financial interests or personal relationships that could have appeared to influence the work reported in this paper.

Acknowledgments

References

[1]   Z.W. Li, S.S. Xie, Large-scale synthesis of aligned carbon nanotubes, Science 274 (1996) 1701-1703. https://doi.org/10.1126/science.274.5293.1701.

[2]   V. Amendola, R. Pilot, M. Frasconi, et al., Surface plasmon resonance in gold nanoparticles: a review, J. Phys. Condens Matter. 29(20) (2017) 203002. https://doi.org/10.1088/1361-648X/aa60f3.

[3]   C.L. Necl, H.W. Liao, J.H. Hafner, Optical properties of star-shaped gold nanoparticles, Nano Lett. 6(4) (2006) 683-688. https://doi.org/10.1021/nl052409y.

[4]   S. Abalde-Cela, P. Aldeanueva-Potel, C. Mateo-Mateo, et al., Surface-enhanced Raman scattering biomedical applications of plasmonic colloidal particles, J. R. Soc. Interface 7(4) (2010) 29. https://doi.org/10.1098/rsif.2010.0125.focus.

[5]   H.Y. Chen, X. Zhang, S.H. Dai, et al., Multifunctional gold nanostar conjugates for tumor imaging and combined photothermal and chemo-therapy, Theranostics 3(9) (2013) 633-649. https://doi.org/10.7150/thno.6630.

[6]   L. Wang, D.H. Meng, Y.W. Hao, et al., Gold nanostars mediated combined photothermal and photodynamic therapy and X-ray imaging for cancer theranostic applications, J. Biomate. Appl. 30(5) (2015) 547-557. https://doi.org/10.1177/0885328215594481.

[7]   N.N Zhao, L.S. Li, T. Huang, et al., Controlled synthesis of PbS-Au nanostar-nanoparticle heterodimers and cap-like Au nanoparticles, Nanoscale 2(11) (2010) 2418-2413. https://doi.org/10.1039/c0nr00385a.

[8]   B. Khlebtsov, E. Panfilova, V. Khanadeev, et al., Improved size-tunable synthesis and SERS properties of Au nanostars, J. Nanopart. Res. 16(10) (2014) 2623. https://doi.org/10.1007/s11051-014-2623-8.

[9]   J. Verma, H.A.V. Veen, S. Lal, et al.,Wet chemistry approaches for synthesis of gold nanospheres, nanorods and nanostars, Curr. Nanosci. 10(5) (2014) 660-669. https://doi.org/10.2174/1573413710666140526232421.

[10] E.C. Hao, R.C. Bailey, G.C. Schatz, et al., Synthesis and optical properties of "branched" gold nanocrystals, Nano Lett. 4(2) (2004) 327-330. https://doi.org/10.1021/nl0351542.

[11] W. Moukarzel, J. Fitremann, J.D. Marty, Seed-less amino-sugar mediated synthesis of gold nanostars, Nanoscale 3(8) (2011) 3285-3290. https://doi.org/10.1039/C1NR10418G.

[12] S. Boca, D. Rugina, A. Pintea, et al., Flower-shaped gold nanoparticles: synthesis, characterization and their application as SERS-active tags inside living cells, Nanotechnology 22(5) (2011) 055702. https://doi.org/10.1088/0957-4484/22/5/055702.

[13] J.V. Jokerst, M. Zheng, C. Zavaleta, et al., Affibody-functionalized gold-silica nanoparticles for Raman molecular imaging of the epidermal growth factor receptor, Small 7(5) (2015) 625-633. https://doi.org/10.1002/smll.201002291.

[14] H. Yuan, Y. Liu, A.M. Fales, et al., Quantitative surface-enhanced resonant Raman scattering multiplexing of biocompatible gold nanostars for *in vitro* and *ex vivo* detection, Anal. Chem. 85(1) (2013) 208-212. https://doi.org/10.1021/ac302510g.

[15] J.P. Xie, Q.B. Zhang, J.Y. Lee, et al., The synthesis of SERS-active gold nanoflower tags for *in vivo* applications, ACS Nano 2(12) (2008) 2473-2480. https://doi.org/10.1021/nn800442q.

[16] P. Pallavicini, C. Bernhard, G. Chirico, et al., Gold nanostars co-coated with the Cu(II) complex of a tetraazamacrocyclic ligand, Dalton Trans. 44(12) (2015) 5652-5661. https://doi.org/10.1039/c4dt03042g.

[17] J.C. Li, R. Cai, N. Kawazoe, et al., Facile preparation of albumin-stabilized gold nanostars for the targeted photothermal ablation of cancer cells, J. Mater. Chem. B 3(28) (2015) 5806-5814. https://doi.org/10.1039/c5tb00633c.

[18] S.L. Zhang, J.C. Zang, H. Chen, et al., Nanomaterials: the size flexibility of ferritin nanocage opens a new way to prepare nanomaterials, Small 13(37) (2017) 1701045. https://doi.org/10.1002/smll.201770199.

[19] S.C. Andrews, P. Arosio, W. Bottke, et al., Structure, function, and evolution of ferritins, J. Inorg. Biochem. 47(3/4) (1992) 161-174. https://doi.org/10.1016/0162-0134(92)84062-R.

[20] X.Y. Liao, S.J. Yun, G.H. Zhao, Structure, function, and nutrition of phytoferritin: a newly functional factor for iron supplement, Crit. Rev. Food Sci. Nutr. 54(10) (2014) 1342-1352. https://doi.org/10.1080/10408398.2011.635914.

[21] P.M. Harrison, P. Arosio, The ferritins: molecular properties, iron storage function and cellular regulation, Biochim. Biophys. Acta 1275(3) (1996) 161-203. https://doi.org/10.1016/0005-2728(96)00022-9.

[22] H. Li, X.Y. Tan, X.Y. Xia, et al., Thermal treatment modified the physicochemical properties of recombinant oyster (*Crassostrea gigas*) ferritin, Food Chem. 314 (2020) 126210. https://doi.org/10.1016/j.foodchem.2020.126210.

[23] R.L. Fan, S.W. Chew, V.V. Cheong, et al., Fabrication of gold nanoparticles inside unmodified horse spleen apoferritin, Small 6(14) (2010) 1483-1487. https://doi.org/10.1002/smll.201000457.

[24] B. Maity, S. Abe, T. Ueno, Observation of gold sub-nanocluster nucleation within a crystalline protein cage, Nat. Commun. 8(1) (2017) 14820. https://doi.org/10.1038/ncomms14820.

[25] C.L. Lu, B. Maity, X. Peng, et al., Design of a gold clustering site in an engineered apo-ferritin cage, Commun. Chem. 5(1) (2022) 39. https://doi.org/10.1038/s42004-022-00651-1.

[26] K.W. Pulsipher, S. Honig, S. Deng, et al., Controlling gold nanoparticle seeded growth in thermophilic ferritin protein templates, J. Inorg. Biochem. 174 (2017) 169-176. https://doi.org/10.1016/j.jinorgbio.2017.06.012.

[27] J.P. Xie, J.Y. Lee, D. Wang, Seedless, surfactantless, high-yield synthesis of branched gold nanocrystals in HEPES buffer solution, Chem. Mater. 19(11) (2007) 2823-2830. https://doi.org/10.1021/cm0700100.

[28] Y.Q.Wang, B. Yan, L.X. Chen, SERS tags: novel opticalnanoprobes for bioanalysis, Chem. Rev. 113(3) (2013) 1391-1428. https://doi.org/10.1021/cr300l120g.

[29] G. Kawamura, Y. Yang, K. Fukuda, et al., Shape control synthesis of multi-branched gold nanoparticles, Mater. Chem. Phys. 115(1) (2009) 229-234. https://doi.org/10.1016/j.matchemphys.2008.11.064.

[30] H.A. Day, D. Bartczak, N. Fairbairn, et al., Controlling the three-dimensional morphology of nanocrystals, CrystEngComm 12(12) (2010) 4312-4316. https://doi.org/10.1039/c0ce00264j.

[31] H. Li, J.C. Zang, X.Y. Tan, et al., Purification and characterizations of a nanocage ferritin GF1 from oyster (*Crassostrea gigas*), LWT-Food Sci. Technol. 127 (2020) 109416. https://doi.org/10.1016/j.lwt.2020.109416.

[32] M. Reyes, M. Piotrowski, S.K. Ang, et al., Exploiting the anti-aggregation of gold nanostars for rapid detection of hand, foot, and mouth disease causing enterovirus 71 using surface-enhanced raman spectroscopy, Anal. Chem. 89(10) (2017) 5373-5381. https://doi.org/10.1021/acs.analchem.7b00066.

[33] S. He, Y.M.E. Kyaw, E.K.M. Tan, et al., Quantitative and label-free detection of protein kinase a activity based on surface-enhanced raman spectroscopy with gold nanostars, Anal. Chem. 90(10) (2018) 6071-6080. https://doi.org/10.1021/acs.analchem.7b05417.

[34] W. Chao, Y.F. Hua, Y.M. Chen, et al., Effect of temperature, ionic strength and 11S ratio on the rheological properties of heat-induced soy protein gels in relation to network proteins content and aggregates size, Food Hydrocoll. 66 (2017) 389-395. https://doi.org/10.1016/j.foodhyd.2016.12.007.

[35] J. Navarrete, C. Siefe, S. Alcantar, et al., Merely measuring the UV-visible spectrum of gold nanoparticles can change their charge state, Nano Lett. 18(2) (2018) 669-674. https://doi.org/10.1021/acs.nanolett.7b02592.

[36] G.B. Sutherland, Infrared analysis of the structure of amino acids, polypeptides and proteins, Adv. Protein Chem. 7 (1952) 291-318. https://doi.org/10.1016/S0065-3233(08)60021-2.

[37] S. Patil, A. Sandberg, E. Heckert, et al., Protein adsorption and cellular uptake of cerium oxide nanoparticles as a function of Zeta potential, Biomaterials 28(31) (2007) 4600-4607. https://doi.org/10.1016/j.biomaterials.2007.07.029.

[38] Q. Cui, L. Wang, G.R. Wang, et al., Ultrasonication effects on physicochemical and emulsifying properties of *Cyperus esculentus* seed (tiger nut) proteins, LWT-Food Sci. Technol. 142(3) (2021) 110979. https://doi.org/10.1016/j.lwt.2021.110979.

[39] Q.Y. Zhao, C. Wu, C.P. Yu, et al., High stability of bilayer nano-emulsions fabricated by Tween 20 and specific interfacial peptides, Food Chem. 340 (2020) 127877. https://doi.org/10.1016/j.foodchem.2020.127877.

[40] Q.Y. Zhao, H. Li, H. Chen, et al., High throughput analysis and quantitation of α-dicarbonyls in biofluid by plasmonic nanoshells enhanced laser desorption/ionization mass spectrometry, J. Hazard Mater. 403 (2021) 123580. https://doi.org/10.1016/j.jhazmat.2020.123580.

[41] P. Senthil Kumar, I. Pastoriza-Santos, B. Rodríguez-González, et al., High-yield synthesis and optical response of gold nanostars, Nanotechnology 19(1) (2008) 015606. https://doi.org/10.1088/0957-4484/19/01/015606.

[42] C.G. Khoury, T. Vo-Dinh, Gold nanostars for surface-enhanced raman scattering: synthesis, characterization and optimization, J. Phys. Chem. C 112(48) (2008) 18849-18859. https://doi.org/10.1021/jp8054747.

[43] Q.Q. Su, X.Y. Ma, J. Dong, et al., A reproducible SERS substrate based on electrostatically assisted APTES-functionalized surface-assembly of gold nanostars, ACS Appl. Mater. Inter. 3(6) (2011) 1873-1879. https://doi.org/10.1021/am200057f.

[44] M. Schuetz, D. Steinigeweg, M. Salehi, et al., Hydrophilically stabilized gold nanostars as SERS labels for tissue imaging of the tumor suppressor p63 by immuno-SERS microscopy, Chem. Commun. 47(14) (2011) 4216-4218. https://doi.org/10.1039/C0CC05229A.

[45] H. Yuan, C.G. Khoury, H. Hwang, et al., Gold nanostars: surfactant-free synthesis, 3D modelling, and two-photon photoluminescence imaging, Nanotechnology 23(7) (2012) 075102. https://doi.org/10.1088/0957-4484/23/7/075102.

[46] H.S. Liang, Q.R. Huang, B. Zhou, et al., Self-assembled zein-sodium carboxymethyl cellulose nanoparticles as an effective drug carrier and transporter, J. Mater. Chem. B 3(16) (2015) 3242-3253. https://doi.org/10.1039/c4tb01920b.

[47] A. J. Gormley, A. Malugin, A. Ray, et al., Biological evaluation of RGDfK-gold nanorod conjugates for prostate cancer treatment, J. Drug. Target 19(10) (2011) 915-924. https://doi.org/10.3109/1061186X.2011.623701.

[48] J.F. Hainfeld, D.N. Slatkin, T.M. Focella, et al.,Gold nanoparticles: a new X-ray contrast agent, Brit. J. Radiol. 79(939) (2007) 248-253. https://doi.org/10.1259/bjr/13169882.

[49] T. Ling, Q.S. Wei, A. Wei, et al., Gold nanorods as contrast agents for biological imaging: optical properties, surface conjugation and photothermal effects, Photochem. Photobiol. 85(1) (2010) 21-32. https://doi.org/10.1111/j.1751-1097.2008.00507.x.